Power uprates
and plant life extension

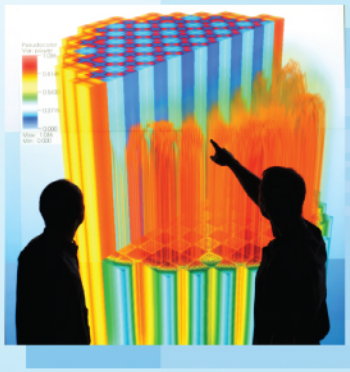

Engineering design
and analysis

Science-enabling
high performance
computing

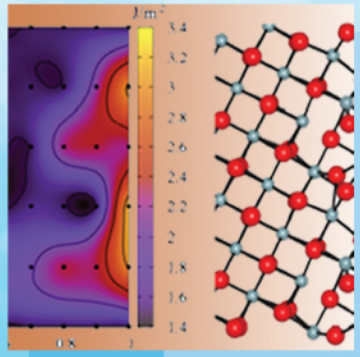

Fundamental science

Plant operational data

Consortium for Advanced Simulation of LWRs

Gen-0 BWR Modeling Application and Validation L3:THM.P18.01

Su-Jong Yoon
Idaho National Laboratory

Emilio Baglietto
Massachusetts Institute of Technology

U.S. DEPARTMENT OF ENERGY | Nuclear Energy

INL/EXT-18-51009
Revision 0

Gen-0 BWR Modeling Application and Validation (L3 Milestone THM.P18.01)

Su-Jong Yoon[1]
Emilio Baglietto[2]

[1]Idaho National Laboratory
[2] Massachusetts Institute of Technology

December 2018

Idaho National Laboratory
Idaho Falls, Idaho 83415

http://www.inl.gov

Prepared by
IDAHO NATIONAL LABORATORY
Idaho falls, ID 83415
for the
U.S. DEPARTMENT OF ENERGY
under contract DE-AC05-00OR22725

CONTENTS

FIGURES

NOMENCLATURE

A_D	Mean linearized drag coefficient	S_{ε_c}	Turbulent dissipation source term
a_{ij}	Interfacial area density	$S_{\bar{i}}^{m}$	Phase mass source term
C_D	Drag Coefficient	$S_{\bar{i}}^{\mathbf{v}}$	Phase momentum source term
c_p	Specific heat	$S_{u,i}$	Energy source term
D_b	Bubble diameter	T	Temperature
d_w	Bubble departure diameter	$\mathbf{T}_i$	Viscous stress tensor
E	Total energy	t_w	Waiting time
F	Interfacial forces	$\mathbf{v}$	Velocity, velocity vector
f	Bubble departure frequency or	y_w	Distance from the wall to the bubble
f_D	Drag correction factor	α	Volume fraction
$\mathbf{F}_{int}$	Internal forces	α_{dry}	Wall dryout break-point
$\mathbf{f}$	Body force vector	ν_c^t	Liquid phase turbulent kinematic viscosity
$\mathbf{g}$	Gravity vector		
H	Total enthalpy	ρ	Density
$h_i(T_{ij})$	Phase i enthalpy at interface temperature T_{ij}	σ_α	Turbulent dispersion Prandtl number
h_{lg}	Latent heat of fluid	$\tau_{\bar{i}}$	Molecular stress
h	Heat transfer coefficient	$\tau_{\bar{i}}^t$	Turbulent stresses
k	Thermal conductivity	χ	Void fraction
K_{dry}	Wall dryout area fraction		
K_{quench}	Quenching influence wall area fraction	***Subscripts***	
$\mathbf{M}_i$	Interphase momentum transfer	D	Drag force
$\dot{m}_{ij}$	Mass transfer rate to phase i from phase j	*eff*	Effective
$\dot{m}_{ji}$	Mass transfer rate to phase j from phase i	g	Vapor phase
n''	Nucleation site density	*in*	inlet
p	Pressure	L	Lift force
Q	Interphase heat transfer rate	l	Liquid phase
q_{conv}	Convective heat flux	*quench*	Quenching
$q_{conv,v}$	Vapor contribution to convective heat flux	*TD*	Turbulent dispersion force
q_{evap}	Evaporative heat flux at wall	*VM*	Virtual mass force
q_{quench}	Quenching heat flux	w	Wall
S_{k_c}	Turbulent kinematic energy source term	*WL*	Wall lubrication force

EXECUTIVE SUMMARY

This milestone report describes the Consortium for Advanced Simulation of Light Water Reactors (CASL) work conducted for completion of the thermal hydraulics Methods (THM) Level 3 milestone L3:THM.P18.01 Gen-0 BWR Modeling Application and Validation.

The extension of existing boiling closure designed for Pressurized Water Reactors (PWRs) to the high void fraction condition of Boiling Water Reactors (BWRs) is one of the challenges for Multiphase Computational Fluid Dynamics (M-CFD) applications. In the efforts aimed at developing the advanced boiling closure for BWRs, the baseline closure model, so-called 'Zero' closure, has been developed by leveraging the experience gained through the Numerical Nuclear Reactor project. This baseline closure model is physics-based, simplest and robust, but it does not contain any explicit descriptions of the complex high void fraction mechanisms. This is a continuation of the CASL thermal-hydraulic study to develop and assess the CFD-BWR models. In FY-17, the applicability has been evaluated against the international OECD/NRC BFBT benchmark data. In the present work, we assessed the capability of CFD-BWR model for void drift phenomena in the modern BWR fuel designs which make use of both full-length and part-length rods.

ACKNOWLEDGEMENTS

This research was supported by the Consortium for Advanced Simulation of Light Water Reactor (www.casl.gov), an Energy Innovation hub (http://www.energy.gov/hubs) for Modeling and Simulation of Nuclear Reactors under U.S. Department of Energy Contract No. DE-AC05-00OR22725.

1. MILESTONE DESCRIPTION

This report describes the Consortium for Advanced Simulation of Light Water Reactors (CASL) work conducted for completion of the Thermal Hydraulic Method (THM) milestone, L3:THM.P18.01. This milestone aims at evaluating modeling capabilities for the Boiling Water Reactor (BWR) applications implemented in the CASL Computational Fluid Dynamics (CFD) code. The Gen-0 BWR closure model, which is so called "zero closure", has been developed by leveraging the experience gained through the Numerical Nuclear Reactor project (Tentner, et al., 2014). The Gen-0 BWR closure model has been benchmarked against the OECD/NRC BWR Full-size Fine-mesh Bundle Test (BFBT) (Neykov, et al., 2006) data in FY-17 (Yoon, Baglietto, & Agostinelli, 2017). This is a continuation of the CASL thermal-hydraulic activities to develop and evaluate the CFD-BWR model. To assess the modeling capability of Gen-0 BWR closure, the CFD model for the Westinghouse FRIGG 5x5 rod bundle with part-length rods has been developed. The milestone required completion of the following tasks:

- Identification of FRIGG 5x5 rod bundle geometry
- Development of CFD model of FRIGG 5x5 rod bundle
- Multi-phase CFD simulation for exit void fraction and quality
- Submission of this milestone report

2. INTRODUCTION

Most modern BWR fuel bundle designs make use of both full-length and part-length rods to improve fuel performance, which results in lattice heterogeneity in the upper part of the bundle. Predicting the flow redistribution in heterogeneous bundles has shown to be particularly challenging. The Westinghouse FRIGG 5x5 rod bundle test results showed that the void in the open channel was always higher than in the closed channel despite much lower power/flow ratio (phenomenon known as "void drift"). The concept of void drift has been proposed by (Jr., Shiralkar, Radcliffe, & Polomik, 1972) based on the experimental observations and ad-hoc modeling. The void drift phenomenon is important for accurate prediction of void distribution because it leads to significant crossflow within the fuel lattice.

Figure 1 shows FRIGG 5x5 test bundle geometry including part-length rods. The test bundle includes a corner 1/3rd PLR, which is 1/3rd of full length rod, four 2/3rd PLRs, 6 full length rods of 3.8 m heated length, a large unheated rod representative of a water channel and 7 spacer grids with mixing vanes along the heated length. The local dynamic pressure and void at the outlet of test section were measured. The sub-channels, instrumentation positions and part-length rods are shown in Fig. 2. The experiment was performed at a pressure of 70.0 bar, inlet sub-cooling of 10.0 ºC and mass flux within the range of 400 to 2000 kg/m^2-sec.

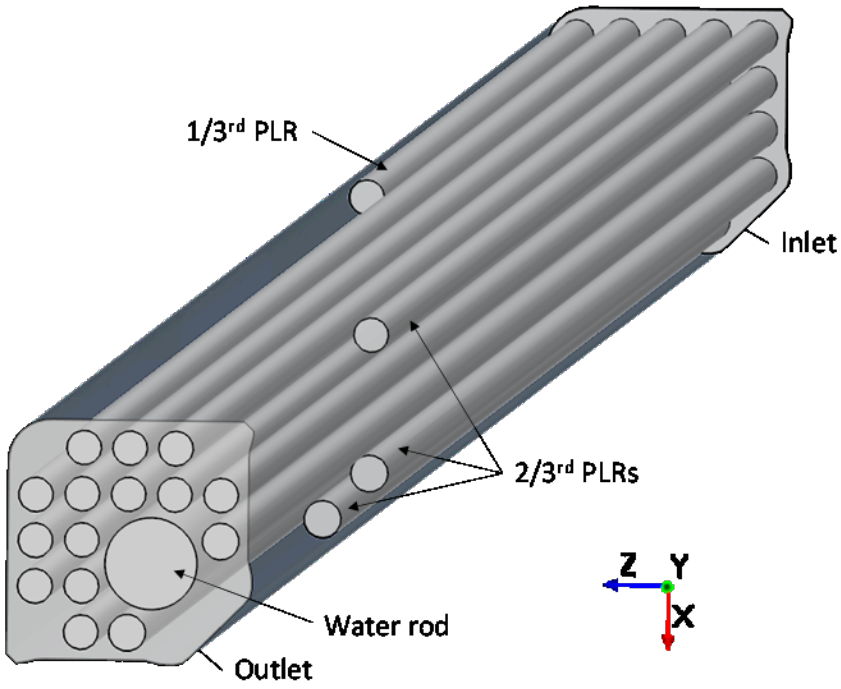

Figure 1. FRIGG 5x5 Test Bundle Geometry.

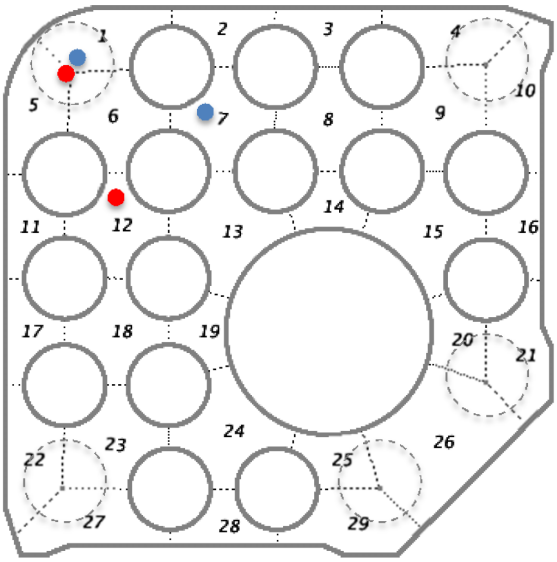

Figure 2. Sub-channel, Instrumentation Positions and PLRs in Test Bundle (Le Corre, 2017)

3. GEN-0 BWR CLOSRE MODEL

The Gen-0 BWR boiling closure model is the baseline closure used in this work to model the physics at the interface between the two phases. It aims at including the simplest and most robust representation of the key mechanisms of the physics of the two-phase flow, rather than aiming at absolute accuracy of the predictions. Gen-0 BWR boiling closure model was implemented in the commercial CFD software *STAR-CCM+ v12.06.011-R8.* Models that were not available in the commercial code were implemented as user-defined field functions. This section reviews the details

of Zero Closure model.

3.1 Transport Equations

The Eulerian-Eulerian (two-fluid) formulation is employed as the M-CFD framework. Detailed descriptions of governing equations can be found in (Simens PLM Software Inc., 2018).

Mass conservation:

$$\frac{\partial}{\partial t}(\alpha_i \rho_i) + \nabla \cdot (\alpha_i \rho_i u_i) = \sum_i (\dot{m}_{ji} - \dot{m}_{ij}) \tag{1}$$

$$\sum_i \alpha_i = 1 \tag{2}$$

Momentum conservation:

$$\frac{\partial}{\partial t}(\alpha_i \rho_i u_i) + \nabla \cdot (\alpha_i \rho_i u_i u_i) - \nabla \cdot \left(\alpha_i (\tau_i + \tau_i^t)\right) = -\alpha_i \nabla p + \alpha_i \rho_i g + M_i \tag{3}$$

Energy conservation:

$$\frac{\partial}{\partial t}(\alpha_i \rho_i e_i) + \nabla \cdot (\alpha_i \rho_i u_i e_i) - \nabla \cdot (\alpha_i \lambda_i \nabla T_i) = Q \tag{4}$$

In order to calculate the continuous and dispersed phase turbulence stresses used in Eqn. (3), the realizable k-ε turbulence model with high y+ wall treatment was employed. Details of Realizable k-ε model implemented in STAR-CCM+ software can be found in (Simens PLM Software Inc., 2018). Troshko-Hassan particle-induced turbulence model (Troshko & Hassan, 2001) is employed as source terms to account for the bubble-induced turbulence with model coefficient, C_3, of 0.45 and damping coefficient of 1.0. The source terms for turbulent kinematic energy and dissipation are given by Eqn. (5) and Eqn. (6), respectively, as follows:

$$S_{k_c} = \frac{3}{4}\frac{C_D}{D_b}\alpha_g \rho_l \left|\mathbf{v}_l - \mathbf{v}_g\right|^3 \tag{5}$$

$$S_{\varepsilon_c} = \frac{C_3 S_{k_c}}{t_b} \tag{6}$$

.

3.2 Gen-0 Closure Model Description

The Eulerian-Eulerian (two-fluid) formulation is employed as the M-CFD framework. Detailed descriptions of governing equations can be found in (Simens PLM Software Inc., 2018) .

3.2.1 Interface Area Density and Interaction Length Scale

Based on the surface area of spherical particle, the interfacial area density is modeled through the use of a Sauter mean diameter d_s (Ishii & Hibiki, 2006) as follows:

$$a_{ij} = 6\alpha_g / d_s \quad (7)$$

The Sauter mean diameter adopts and algebraic formulation to describe the interfacial variation among different flow regimes. The Sauter mean diameter given by Eqn. (8) is implemented in STAR-CCM+ by means of user-defined function.

$$d_s = \begin{cases} 10.06(p/p_0)^{-0.098}\sqrt{\sigma/\Delta\rho g}\left[\min(\alpha_g, 0.118)\right]^{0.35} & \alpha_g < 0.4 \\ 1.9425\times10^{-3}\exp(2.3637\alpha_g) & 0.4 < \alpha_g < 0.8 \\ 0.864 D_h & 0.8 < \alpha_g \end{cases} \quad (8)$$

The Yoneda correlation (Yoneda, Yasuo, & Okawa, 2002) is used for the bubbly flow regime, when void fraction, α_g is less than 0.4. An exponential trend is chosen for the intermediate flow regimes ($0.4 \leq \alpha_g < 0.8$), while the channel hydraulic diameter D_h is used as the characteristic length scale in the annular flow region ($\alpha_g \geq 0.8$) and has a numerical constant value of 0.01 for this application.

3.2.2 Wall Heat Partitioning Model

In order to represent the heat transfer between the heated wall and the fluid and the boiling at the wall, a previously validated form of the classic Kurul-Podowski mechanistic heat partitioning is applied (Baglietto & Christon, 2013). The wall heat flux consists of three components as follows:

$$q''_w = \left(q''_{conv} + q''_{evap} + q''_{quench}\right)\left(1 - K_{dry}\right) + K_{dry} q''_{dry} \quad (9)$$

For liquid contact with the wall, the convective heat flux is given by:

$$q''_{conv} = \frac{\rho_l c_{pl} u_l^*}{t_l^+}\left(T_w - T_l\right) \quad (10)$$

For vapor contact with the wall, the convective heat flux is given by:

$$q''_{dry} = \frac{\rho_g c_{pg} u_g^*}{t_g^+}\left(T_w - T_g\right) \quad (11)$$

The wall contact area fraction (Simens PLM Software Inc., 2018) is given by:

$$K_{dry} = \begin{cases} 0 & \alpha_\delta \leq \alpha_{dry} \\ \beta^2(3-2\beta) & \alpha_{dry} < \alpha_\delta \end{cases} \quad (12)$$

$$\beta = \frac{\alpha_\delta - \alpha_{dry}}{1 - \alpha_{dry}} \quad (13)$$

where α_δ is the vapor volume fraction averaged over the bubbly layer thickness and α_{dry} is the wall dryout break-point with default value of 0.9. The cell-center volume fraction is used in the dryout criterion by selecting "Wall Cell" option for specifying the bubble layer thickness.

The evaporative heat flux is determined as follows:

$$q''_{evap} = n'' f\left(\frac{\pi d_w^3}{6}\right)\rho_g h_{fg} \quad (14)$$

In this work, Lemmert-Chawla model (Lemmert & Chawla, 1977) (Podowski & Podowski, 2009)for nucleation site number density given by Eqn.(15), Cole model (Cole, 1960) for bubble departure frequency given by Eqn.(16) and Tolubinsky-Kostanchuk model (Tolubinsky & Kostanchuk, 1970) for bubble departure diameter given by Eqn.(17) were employed to calculate the evaporative heat flux. Note that the Lemmert-Chawla nucleation site number density model and Tolubinsky-Kostanchuk bubble departure diameter model should be used together to form the effective boiling area because these correlations were tuned as one model against measured data for a wide range of conditions (Lo & Osman, 2012). Lemmert-Chawla nucleation site number density is given by:

$$n'' = \left(m\Delta T_{sup}\right)^p \quad (15)$$

where m=185.0 (1/K), p=1.805 and ΔT_{sup} is the wall superheat.

Cole bubble departure frequency is given by:

$$f = \sqrt{\frac{4}{3}\frac{g(\rho_l - \rho_g)}{d_w \rho_l}} \quad (16)$$

Tolubinsky-Kostanchuk bubble departure diameter is given by:

$$d_w = d_0 \exp\left[-\frac{\Delta T_{sub}}{\Delta T_0}\right] \quad (17)$$

where d_0 is the reference diameter with default value of 0.6 mm, ΔT_0 is the reference subcooling with default value of 45 K and ΔT_{sub} is the subcooling of the liquid. The minimum and maximum values of bubble departure diameter were specified by 0.025 mm and 1.4 mm, respectively.

The quenching heat flux is obtained by Eqn. (18) using the Del Valle Kenning model (Valle & Kenning, 1985) for bubble induced quenching heat transfer coefficient given by Eqn. (19).

$$q''_{quench} = h_{quench}\left(T_w - T_{quench}\right) \quad (18)$$

The quenching heat transfer coefficient is determined by the Del Valle Kenning model as follows:

$$h_{quench} = 2K_{quench} f \sqrt{\frac{\rho_l c_{pl} k_l t_w}{\pi}} \quad (19)$$

where K_{quench} is the bubble influence wall area fraction, f is the bubble departure frequency, t_w is the waiting time between the bubble departure and the nucleation of the next bubble with wait coefficient of 0.8.

The bubble influence wall area fraction is obtained using Kurul-Podowski model (Kurul & Podowski, 1990) as follows:

$$K_{quench} = C_A \frac{\pi d_w^2}{4} n'' \tag{20}$$

where C_A is the area coefficient for scaling between the nucleation site area density and the wall area fraction the bubble-induced quenching influences with the default value of 2.0.

3.2.3 Interphase Momentum Transfer Models

The interphase momentum transfer term, $\mathbf{M}_i$, represents the sum of all the liquid-vapor interfacial forces. The interphase momentum transfer term includes contributions from the drag force, virtual mass force, lift force, turbulent dispersion force and wall lubrication force as follows:

$$\mathbf{M}_i = F_D + F_{VM} + F_L + F_{TD} + F_{WL} \tag{21}$$

where F_D is the drag force term, F_{VM} is the virtual mass force term, F_L is the lift force term, F_{TD} is the turbulent dispersion force term and F_{WL} is the wall lubrication force term.

The drag force term acting on the vapor phase due to the liquid phase is given in Eqn. (22). Tomiyama correlation (Tomiyama, Kataoka, Zun, & Kakaguchi, 1998) for a drag coefficient and the volume fraction exponent drag correction were used to calculate the drag force. Details of volume fraction exponent drag correction can be found in (Simens PLM Software Inc., 2018).

$$F_D = f_D C_D \frac{1}{2} \rho_l (\mathbf{v}_l - \mathbf{v}_g) |\mathbf{v}_l - \mathbf{v}_g| (a_{\bar{g}}/4) \tag{22}$$

The virtual mass force is given by Eqn. (23) with a spherical particle virtual mass coefficient, C_{VM}, of 0.5.

$$F_{VM} = C_{VM} \rho_l \alpha_g \left(\frac{D\bar{u}_l}{Dt} - \frac{D\bar{u}_g}{Dt} \right) \tag{23}$$

The lift force term is given by Eqn. (24). While accurate lift closure are being developed, current work has evidenced the inapplicability of existing correlations (Sugrue & Baglietto, 2015). The lift closure is leveraged to reproduce the key physical effect of bubble migration through a simple step function for lift coefficient given by Eqn. (25). A positive and constant value of 0.025 is used for α_g<0.25, representing almost spherical bubbles in the low void fraction regime, which accumulate near the wall; while a negative constant value of -0.025 for $\alpha_g \geq 0.25$, representing larger wobbly bubbles that migrate towards the center of the channel.

$$F_L = C_L \rho_l \alpha_g (\mathbf{v}_r \times (\nabla \times \mathbf{v}_l)) \tag{24}$$

$$C_L = \begin{cases} 0.025 & \alpha_g \leq 0.25 \\ -0.025 & 0.25 < \alpha_g \end{cases} \tag{25}$$

The turbulent dispersion force term is given by Eqn. (26) in a logarithmic form (Simens PLM Software Inc., 2018).

$$F_{TD} = A_D \frac{\nu_l^t}{\sigma_\alpha}\left(\nabla \ln(\alpha_l) - \nabla \ln(\alpha_g)\right) \tag{26}$$

where A_D is the mean linearized drag coefficient evaluated using a mean slip velocity and mean interfacial area, ν_c^t is the liquid phase turbulent kinematic viscosity and σ_α is the turbulent dispersion Prandtl number which was set to 1.0.

The wall lubrication force model given in Eqn. (27) is proposed by Antal et al. (Antal, Lahey, & Flaherty, 1991) In this study, the wall lubrication formulation is employed with the calibration coefficients C_{w1} of -0.01 and C_{w2} of 0.05.

$$F_{WL} = -\alpha_g \rho_l \frac{\left|\mathbf{v}_g - \mathbf{v}_l\right|^2}{D_b} \max\left\{\left(C_{w1} + C_{w2}\frac{D_b}{y_w}\right), 0\right\}\mathbf{n} \tag{27}$$

3.2.4 Interphase Mass Transfer Model

A correlation for the Nusselt number for each phase at the interface is required to model bulk boiling and condensation. Since the difference in temperature between the interface and the vapor phase is not significant, a constant value of Nusselt number for vapor phase was specified as 2.0, while Chen-Mayinger model (Chen & Mayinger, 1992) given by Eqn. (28) is employed to determine the continuous phase Nusselt number.

$$Nu_l = 0.185\,\mathrm{Re}_g^{0.7}\,\mathrm{Pr}_l^{0.5} \tag{28}$$

4. ASSESSMENT OF M-CFD CAPABILITY

The CFD model of Westinghouse FRIGG 5x5 rod bundle has been developed to evaluate the CASL BWR M-CFD model capabilities. Since the FRIGG data is a proprietary of Westinghouse, this report does not include any specific dimensions of rod bundle geometry and design except for the information can be found from the literatures.

4.1 CFD Model Description

This section describes the CFD model of FRIGG 5x5 rod bundle. Figure 3 shows the mesh structure of CFD model. A hexa-dominant trimmed mesh, in combination with boundary fitted prism layers was generated with the built-in mesh generation function of STAR-CCM+. In this work, the spacer grids are not modeled because spacer grid geometry has not been provided. The uniform cell size of 2.0 mm is employed away from the wall, while the prism boundary layer total thickness was specified to be 0.5 mm, and two boundary layers were implemented to guarantee a y+ value from the near wall cell between 86.8 to 175.8. Note that the M-CFD model with small y+ value would not be robust for high void fraction conditions. The total number of computational cells was 3.7 million. The reference pressure and inlet subcooling of CFD analysis are the same as the experimental conditions. The pressure of the model is 70.0 bar and inlet subcooling is 10 ºC. The inlet velocity was ranged from 1.0 m/s to 2.704 m/s, which correspond to the inlet mass flux of 740 kg/m^2-s and 2,000 kg/m^2-s, respectively. The heating power of rod bundle in the CFD simulation was varied in the range from 300 kW to 1,000 kW. Cosine shape axial power profiles for both full-length and part-length rods were imposed as seen in Fig. 4. Non-uniform radial power profile of rods was employed. The parallelized simulation was performed with 500 processors on High Performance Computing

(HPC) cluster, *Falcon*, at Idaho National Laboratory (INL).

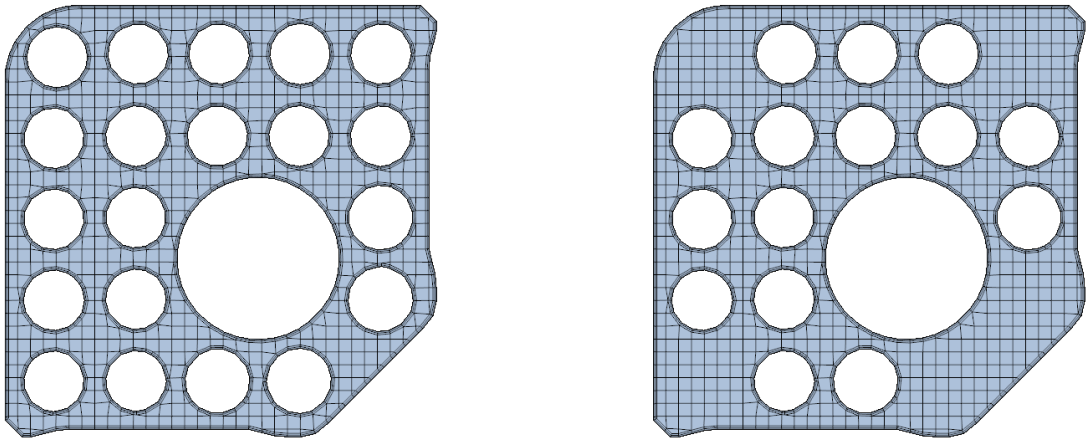

(a) Mesh structure at the inlet **(b) Mesh structure at the outlet**

Figure 3. Mesh Structure of FRIGG 5x5 Rod Bundle

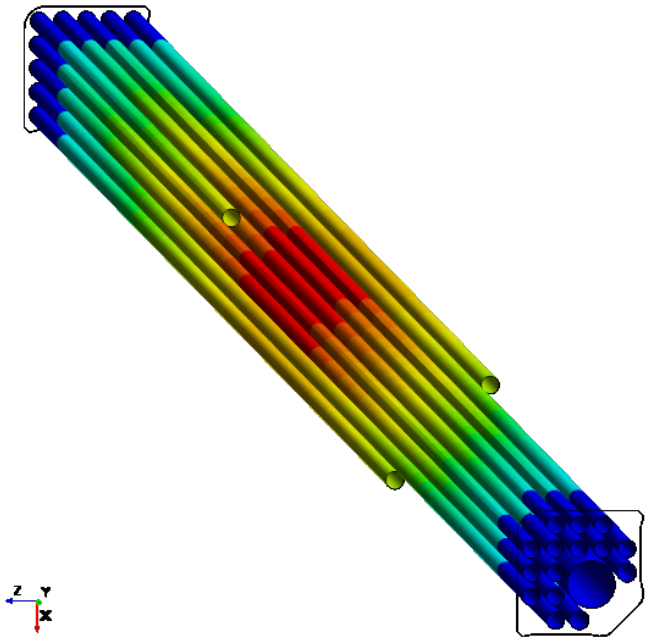

Figure 4. Axial Power Profile

4.2 Local Void Distribution and Phase Velocities

Figure 5 shows the local void distribution and phase velocities measured at the end of heated length in the FRIGG 5x5 rod bundle tests (Le Corre, 2017). In this experiment, the measured local void fraction at the open-channel downstream the corner PLR was always higher than that at the closed channel despite of that the open-channel has significantly lower power-to-flow ratio than closed channel. The local void fractions at the center of open-channel and the closed-channel was analyzed to evaluate the Gen-0 closure model against the experiment.

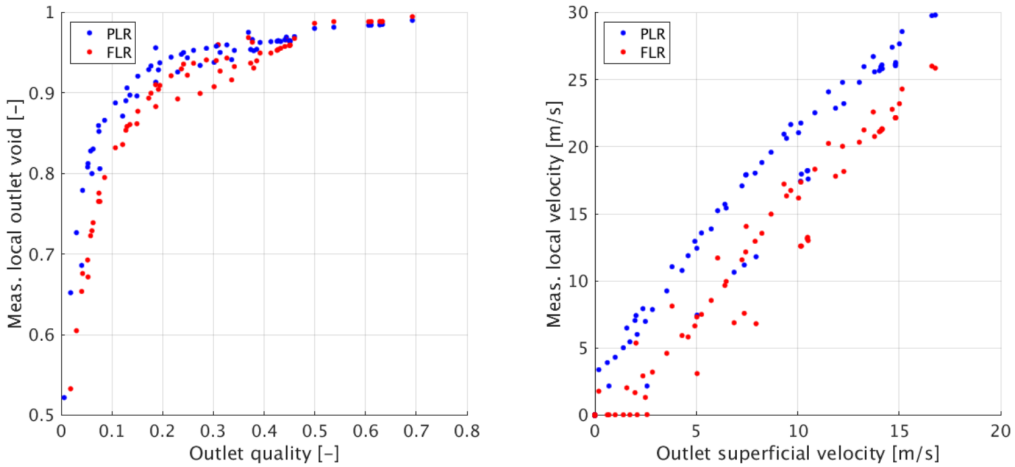

Figure 5. Westinghouse FRIGG 5x5 Rod Bundle Experimental Results (Le Corre, 2017)

Figure 6 shows the local void fractions of open-channel and closed-channel at the outlet of rod bundle. Contrary to the experimental data, the local void fraction of the open-channel was lower than that of closed-channel regardless of the inlet flow velocity condition.

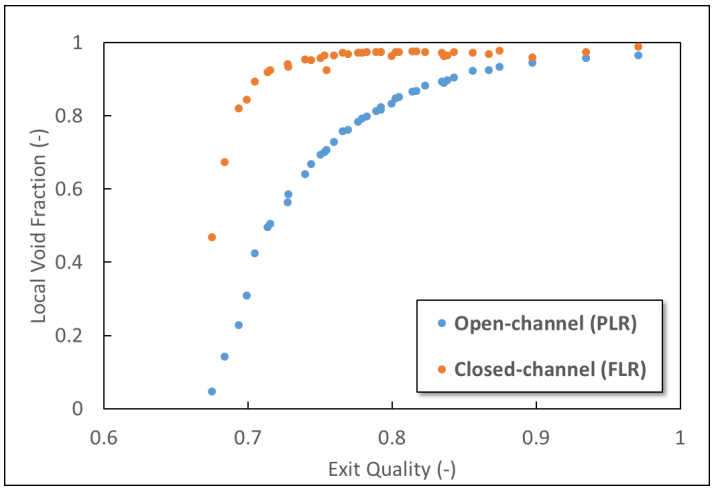

Figure 6. CFD Result of Local Void Fractions at the Outlet of Rod Bundle

The vapor velocity at the open-channel was higher than that at the closed channel when the exit quality is greater than 0.8. Contrary to the experimental data, the differences in vapor velocity at the open-channel and closed-channel was small.

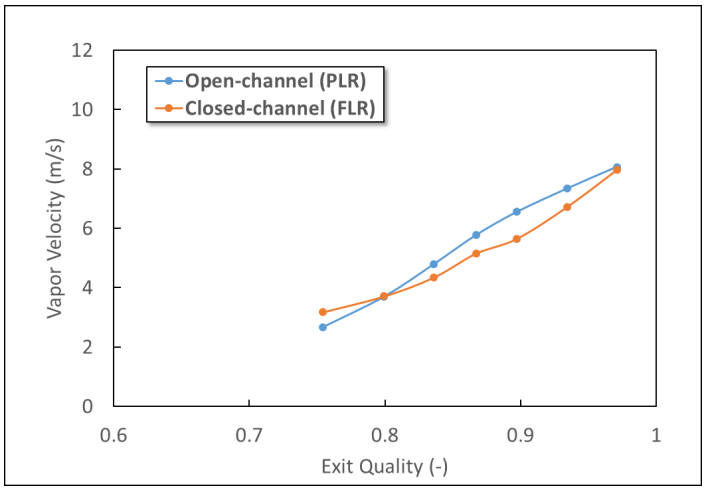

Figure 7. CFD Result of Local Vapor Velocities at the Outlet of Rod Bundle (V_{in}=1.0 m/s)

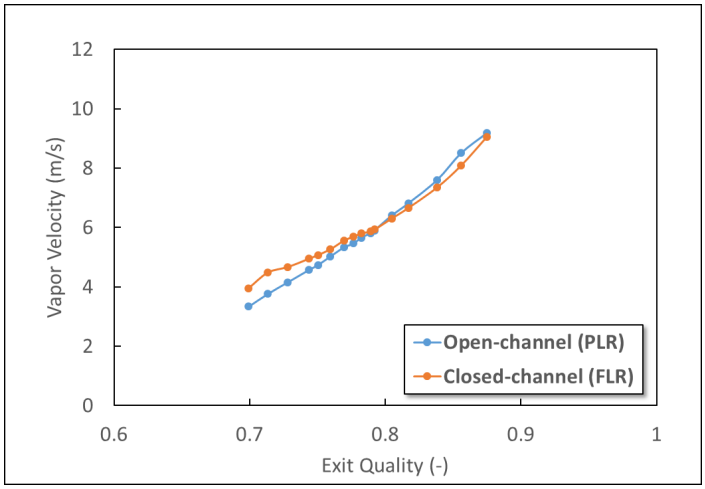

Figure 8. CFD Result of Local Vapor Velocities at the Outlet of Rod Bundle (V_{in}=2.0 m/s)

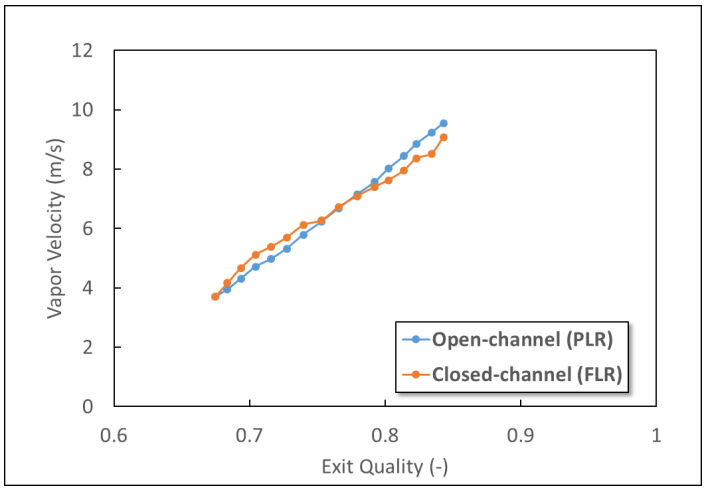

Figure 9. CFD Result of Local Vapor Velocities at the Outlet of Rod Bundle (V_{in}=2.704m/s)

Figures 10 and 11 show the void distributions at the end of heated length (EHL) and outlet of rod bundle for the heating powers of 300 kW and 1000 kW. For both heater powers of 300 kW and 1000 kW, lateral movement of void from the closed-channel to open-channel was observed. Since there is no heating from the EHL, increasing void fraction at the open-channel would be caused by the equilibrium void distribution and/or the void drift. The tangential velocity vector field of liquid flow in Fig. 12-(a) showed that the liquid flow would not lead to the lateral void movement from closed-channel to open-channel. The lateral vapor velocity vector from closed-channel to open-channel was observed as shown in Fig. 12-(b). Although the vapor migration from closed-channel to open-channel was observed, there is significant difference in the local void fraction between the CFD result and experimental data. One of the possible reasons for this difference would be the spacer grid effect. Since the spacer grids were not modeled in current CFD model, the flow mixing characteristics in the rod bundle could be very different from the experiment. Another possible reason would the interfacial force term effect. It deemed that the current interfacial momentum transfer models of Gen-0 closure model cannot result in a sufficient void migration to larger area. Hence, further work would need to examine the effect of spacer grid modeling and capability of Gen-0 closure model.

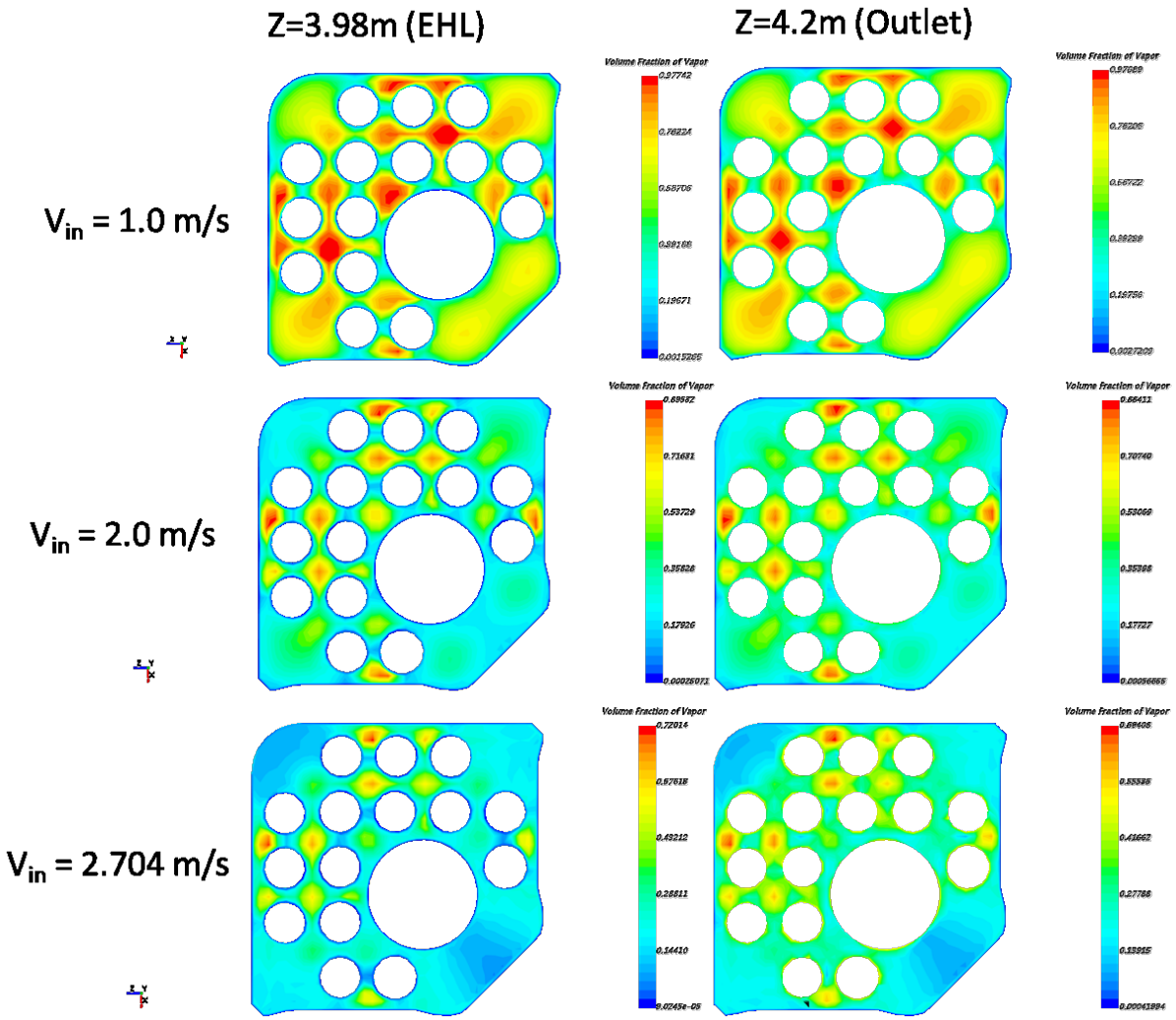

Figure 10. Void Distributions at the End of Heated Length and Outlet of Rod Bundle (P=300 kW)

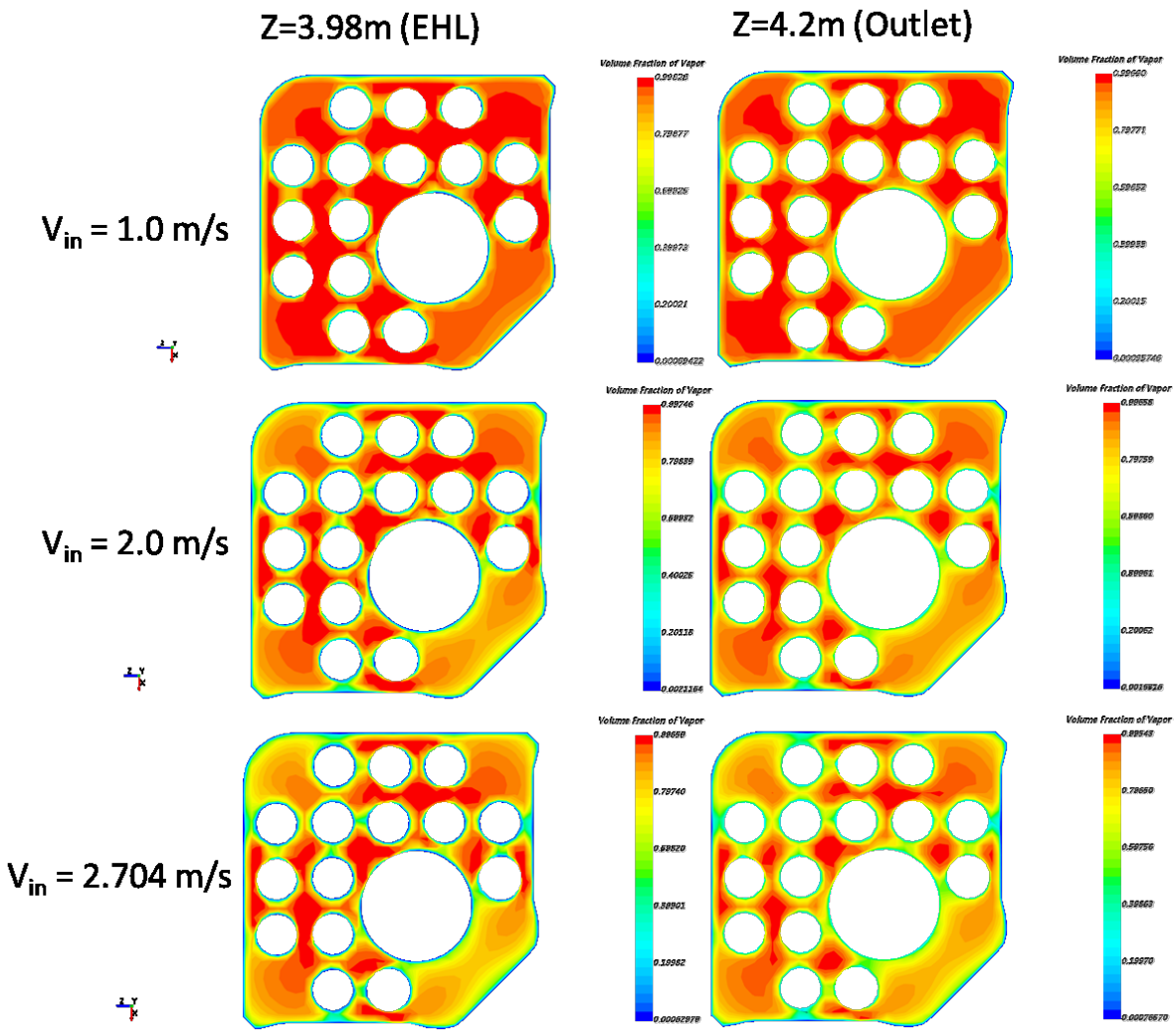

Figure 11. Void Distributions at the End of Heated Length and Outlet of Rod Bundle (P=1000 kW)

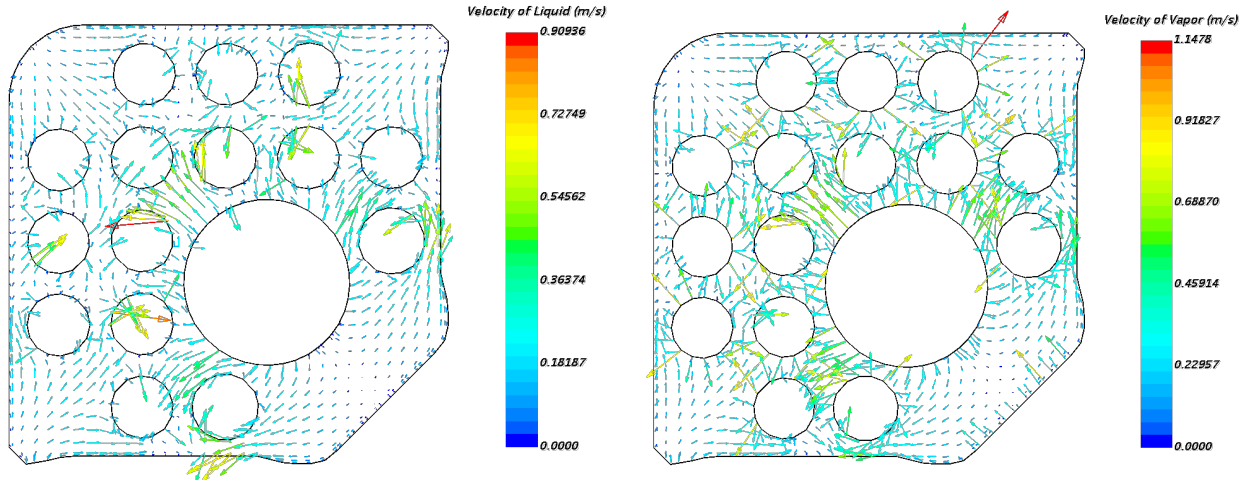

(a) Liquid Velocity Vector (b) Vapor Velocity Vector

Figure 12. Tangential Velocity Vector Fields at the Outlet of Rod Bundle (Vin = 2.0 m/s, P =1000 kW)

5. CONCLUSIONS

In this milestone report, the modeling capability of CASL M-CFD with the Gen-0 closure for the void drift phenomenon has been demonstrated. The CFD benchmark against the Westinghouse 5x5 FRIGG rod bundle test disagreed with experimental data. In the CFD analysis, the local void fraction at the closed-channel was higher than that at the open-channel which is the opposite trends of experimental data. It is unfortunate that this CFD model did not include the spacer grids geometry which can have a significant impact on the void distribution. In addition, it deemed that the current interfacial momentum transfer closures model cannot result in the sufficient void migration from closed-channel to open-channel. In summary, further study needs to be done to examine the effect of spacer grid and to develop a robust and accurate closure model.

REFERENCES

Antal, S., Lahey, R., & Flaherty, J. (1991). Analysis of Phase Distribution in Fully Developed Laminar Bubbly Two-phase Flow. *Int. J. Heat Mass Transfer, 17*, 635-652.

Baglietto, E., & Christon, M. (2013). *Demonstration and Assessment of Advanced Modeling Capabilities for Multiphase Flow with Sub-cooled Boiling.* CASL-U-2013-0181-001.

Chen, Y., & Mayinger, F. (1992). Measurement of Heat Transfer at Phase Interface of Condensing Bubble. *Int. J. Multiphase Flow, 18*, 877-890.

Cole, R. (1960). A Photographic Study of Pool Boiling in the Region of the Critical Heat Flux. *AIChe J., 6*, 533-542.

Ishii, M., & Hibiki, T. (2006). *Thermo-Fluid Dynamics of Two-Phase Flow.* New York, USA: Springer.

Jr., R. L., Shiralkar, B., Radcliffe, D., & Polomik, E. (1972). Out-of-Pile Subchannel Measurements in a Nine-rod Bundle for Water at 1000 psia. *Progress in Heat and Mass Transfer, 6*, 345-362.

Kurul, N., & Podowski, M. (1990). Multidimensional Effects in Subcooled Boiling. *Proceedings of the 9th Heat Transfer Conference.* Jerusalem, Israel.

Le Corre, J.-M. (2017). Experimental Investigation and Modeling of Void Drift in Modern BWR Fuel Designs. *17th International Topical Meeting on Nuclear Reactor Thermal Hydraulics (NURETH-17).* Xi'an, China.

Lemmert, M., & Chawla, J. (1977). Influence of Flow Velocity on Surface Boiling Heat Transfer Coefficient. *Heat Transfer in Boiling*, 237-247.

Lo, S., & Osman, J. (2012). CFD Modeling of Boiling Flow in PSBT 5x5 Bundle. *Science and Technology of Nuclear Installations, 2012*, Article ID 795935, 8 pages.

Neykov, B., Aydogan, F., Hochreiter, L., Ivanov, K., Utsuno, H., Kasahara, K., . . . Martin, M. (2006). *Nupec BWR Full-size Fine-mesh Bundle Test (BFBT) Benchmark, Volume I: Specification.* OECD NEA.

Podowski, M., & Podowski, R. (2009). Mechanistic Multidimensional Modeling of Forced Convection Boiling Heat Transfer. *Science and Technology of Nuclear Installations*, Article ID387020, 10pages.

Simens PLM Software Inc. (2018). *STAR-CCM+ User Guide.* Retrieved from STAR-CCM+ User Guide: https://mdx.plm.automation.siemens.com/star-ccm-plus

Sugrue, R., & Baglietto, E. (2015). A reevaluation of the Lift Force in Eulerian Multiphase CFD. *The 16th International Topical Meeting on Nuclear Reactor Thermal Hydraulics.* Chicago, IL.

Tentner, A., Lo, S., Ioilev, A., Samigulin, M., Ustinenko, V., & Kozlov, V. (2014). Advances in Computational Fluid Dynamics Modeling of Two-phase Flow in a Boiling Water Reactor Fuel Assembly. *Proceedings of the 14th International Conference on Nuclear Engineering (ICONE-14).* Miami, FL.

Tolubinsky, V., & Kostanchuk, D. (1970). Vapour Bubbles Growth Rate and Heat Transfer Intensity at Subcooled Water Boiling. *Heat Transfer, 5*, Paper No. B-2.8.

Tomiyama, A., Kataoka, I., Zun, I., & Kakaguchi, T. (1998). Drag Coefficients of Single Bubbles under Normal and Micro Gravity Conditions. *JSME International Journal, Series B, 41*(2), 472-479.

Troshko, A., & Hassan, Y. (2001). A two-equation turbulence model of turbulent bubbly flows. *International Journal of Multiphase Flow, 27*, 1965-2000.

Valle, M. D., & Kenning, D. (1985). Subcooled Flow Boiling at High Heat Flux. *Int. J. Heat Mass Transfer, 28*, 1907-1920.

Yoneda, K., Yasuo, A., & Okawa, T. (2002). Flow Structure and Bubble Characteristics of Steam-water Two-phase Flow in a Large-diameter Pipe. *Nuclear Engineering and Design, 217*, 267-281.

Yoon, S., Baglietto, E., & Agostinelli, G. (2017). *BWR Full Fuel Assembly Testing and Validation.* Idaho Falls: Idaho National Laboratory.